

Hierarchically self-assembled homochiral helical microtoroids

Received: 24 November 2021

Accepted: 7 September 2022

Published online: 3 November 2022

 Check for updates

Cong Du^{1,3}, Zujian Li^{1,3}, Xuefeng Zhu¹, Guanghui Ouyang¹✉ and Minghua Liu^{1,2}✉

Fabricating microscale helical structures from small molecules remains challenging due to the disfavoured torsion energy of twisted architectures and elusive chirality control at different hierarchical levels of assemblies. Here we report a combined solution–interface-directed assembly strategy for the formation of hierarchically self-assembled helical microtoroids with micrometre-scale lengths. A drop-evaporation assembly protocol on a solid substrate from pre-assembled intermediate colloids of enantiomeric binaphthalene bisurea compounds leads to microtoroids with preferred helicity, which depends on the molecular chirality of the starting enantiomers. Collective variable-temperature spectroscopic analyses, electron microscopy characterizations and theoretical simulations reveal a mechanism that simultaneously induces aggregation and cyclization to impart a favourable handedness to the final microtoroidal structures. We then use monodispersed luminescent helical toroids as chiral light-harvesting antenna and show excellent Förster resonance energy transfer ability to a co-hosted chiral acceptor dye, leading to unique circularly polarized luminescence. Our results shed light on the potential of the combined solution–interface-directed self-assembly approach in directing hierarchical chirality control and may advance the prospect of chiral superstructures at a higher length scale.

Chirality is a universal phenomenon in nature and significantly affects the properties of both biomaterials and artificial materials^{1–4}. The topology of hierarchical chiral architectures^{5–8}, together with their chirality control across length scales⁹, plays a vital role in defining their diverse functionalities. Compared with widely reported chiral superstructures such as fibre bundles, tubes and helices^{10–13}, self-assembled chiral toroidal structures remain largely unexplored due to their conformational constraints regarding circularity and helicity¹⁴. However, in biological systems, a hierarchical self-assembly mechanism involving the precise arrangement of building blocks and masterly control of chirality plays an important role in the formation of chiral circular bioarchitectures from nanoscales to macroscales. For example, the crystal structure of the light-harvesting antenna complex (LH2) shows that the protein

subunits enclosing the pigment molecules unidirectionally assemble into helical ring-shaped topology, which contributes to exciton delocalization within the toroidal π -aggregates and enhances the energy transfer efficiency¹⁵. Another exquisite natural ring structure with larger size is the hierarchically organized coccolith skeletons wherein nanometre-sized calcium carbonate skeletal plates are helically oriented into micrometre toroids¹⁶. Inspired by these amazing naturally occurring helical toroids in living systems, the preparation of helical ring architectures has gained increasing interest among chemistry, materials and biology communities^{17–23}. Despite the fact that the accurate asymmetric synthesis of homochiral molecular macrocycles or toroids has earned credit²⁴, the development of their chiral supramolecular analogues at a higher level of hierarchy (such as micrometre

¹Beijing National Laboratory of Molecular Sciences and CAS Key Laboratory of Colloid, Interface and Thermodynamics, Institute of Chemistry, Chinese Academy of Sciences, Beijing, China. ²University of Chinese Academy of Sciences, Beijing, China. ³These authors contributed equally: Cong Du, Zujian Li. ✉e-mail: ouyanggh@iccas.ac.cn; liumh@iccas.ac.cn

scale) through a self-assembly approach is still in its infancy²⁵, mainly due to the lack of efficient cyclization strategies and remaining challenges in the precise chirality control at higher length scales^{9,26}.

Interfacial self-assembly has proven its capabilities of developing unique topological structures and reconfigurable materials across several length scales owing to interfacial tension and increased morphological stability on substrates^{27–31}. Interestingly, molecular chirality has also been found to profoundly affect the nanostructures of interfacial assemblies of amphiphilic surfactants and rod-like viruses by the chiral control of interfacial tension³². Although advances have been achieved in the preparation of ring structures by the self-organization of linear polymers, discrete organic molecules and nanoparticles on solvent evaporation on a surface^{33,34}, most of these interfacial assemblies are at the nanoscale and are prevalently achiral or mixtures of conglomerates owing to insufficient hierarchical chirality control. Encouraged by our previous progress in the aqueous preparation of helicity-controlled Möbius strips with diameters of 0.5–2.5 μm (ref. ³⁵), we conjecture that the re-assembly of pre-formed nanoscale molecular aggregates on a two-dimensional surface might increase the possibility of their circular stacking due to the reduced degree of freedom and chiral control of interfacial tension, leading to the formation of helical toroids with a larger length scale and favourable size dispersity.

Here we report a combined solution–interface-directed assembly approach to hierarchically construct micrometre-scale helical toroids from amphiphilic binaphthalene bisurea (BU) enantiomers on varied substrates. Morphological analyses reveal that these microtoroidal architectures are composed of helically arranged nanorod-like subunits with an average length of about 420 nm, originating from the interfacial fusion and re-assembly of intermediate solution aggregates. Our molecular dynamics (MD) simulation studies indicate that the pre-assembled molecular aggregates could act as new building blocks to further helically stack on top of each other, leading to the formation of helical microtoroids. The toroidal organization of intermediate aggregates affects the overall chiroptical properties of interfacial assemblies, supporting a microscopic-chirality-regulated structure–property relationship. We then show that the helical microtoroid can be used as a template to accommodate acceptor dye molecules. An efficient excitation energy transfer from donor BU to the chiral acceptor is thus achieved, representing a proof-of-concept light-harvesting antenna with both chirality and circularly polarized light features.

Preparation of homochiral helical microtoroids

To construct helical microtoroids, a combined solution–interface-directed self-assembly strategy is proposed, which involves the stepwise self-assembly of the target compounds into molecular aggregates in solution and subsequent interfacial organization into microtoroids. For this purpose, amphiphilic binaphthalene BU enantiomers (Fig. 1a and Supplementary Scheme 1) comprising a luminescent π -chromophore, two urea moieties and two long alkyl chains were synthesized and fully characterized. These structural subcomponents encode chiroptical properties and unique self-assembly capabilities into the BU molecules, which were indirectly elaborated by a series of reference BU derivatives with alkyl chains of different lengths and methyl-substituted urea groups (Supplementary Scheme 2). BU was first investigated by two-dimensional correlation spectroscopy nuclear magnetic resonance (COSY-NMR) and selective 1D rotating-frame Overhauser effect spectroscopy (ROESY) NMR spectroscopy, and well-resolved proton signals on naphthalene were assigned (Supplementary Figs. 1 and 2). Geometry-optimized structure of (S)-BU by density functional theory (DFT) computation supported the existence of intramolecular hydrogen bonds between two urea groups, leading to a folded conformation of the two long alkyl chains and a binaphthalene dihedral angle of about 74.6° (Supplementary Figs. 3 and 4).

In a typical experimental protocol, the BU samples were dispersed in selected solvents, and the mixture was then heated to 343 K to afford

a transparent supersaturated solution. The subsequent cooling of the BU hot solution to room temperature at a given speed (5 K min⁻¹) was expected to yield intermediate molecular aggregates, which were then immediately transferred onto a two-dimensional surface via a syringe to allow their possible interfacial re-organization on ambient evaporation (Fig. 1b). Self-assembly conditions including solvent type, cooling rate and concentration were found to affect the morphologies of interfacial assemblies. Various solvents from non-polar CCl₄ to polar dimethyl sulfoxide and protic solvents, namely, methanol (MeOH) and ethanol, were screened to evaluate the solvent effect (Supplementary Figs. 7 and 8). Micrometre-sized interfacial toroidal structures were successfully observed for MeOH, and therefore, this solvent was selected for further experimental optimizations. A proper concentration (4 mM in MeOH) was critical to form adequate interfacial BU microtoroids (Supplementary Fig. 9). The cooling rate is another important parameter in defining the supramolecular morphology as well as its functions³⁶. Both slow cooling (1 K min⁻¹) and fast cooling (10 K min⁻¹) failed to yield helical microtoroids with satisfactory dispersity (Supplementary Figs. 10 and 11). The length of the alkyl chains and urea hydrogen bonds of the BU molecules also played important roles in controlling the interfacial self-assembled structures. Semi-spherical or spherical microstructures were obtained for BU derivatives with shortened alkyl chains ((S)-BU-C4, (S)-BU-C7 and (S)-BU-C12; chemical structures shown in Supplementary Scheme 2), whereas microdisc structures were formed for a BU derivative with methyl-protected urea groups ((S)-BU-Me; chemical structure shown in Supplementary Scheme 2), demonstrating the indispensable and collaborative roles of each subcomponent in BU molecules (Supplementary Fig. 13).

Under optimized conditions (4 mM BU in MeOH, cooling from 343 to 293 K at the speed of 5 K min⁻¹), uniform-sized and large-scale microtoroids were successfully obtained on a silica wafer substrate, as observed from both scanning electron microscopy (SEM) and fluorescence microscopy images (Fig. 1c–e). A magnified SEM image of (S)-BU microtoroid clearly showed that the toroidal-shaped superstructure consisted of several dozens of clockwise-oriented nanorod-like subunits, showing left-handed helicity (Fig. 1d), which was further supported by transmission electron microscopy (TEM) and atomic force microscopy images (Supplementary Fig. 14). The helicity preference of these microtoroids followed the molecular chirality of BU molecules, that is, *M*-helical and *P*-helical microtoroids could be successfully obtained from (S)-BU and (R)-BU enantiomers, respectively (Fig. 1c, f and Supplementary Fig. 15). In sharp contrast, racemic BU (*rac*-BU) molecules only resulted in the formation of achiral microplates (Fig. 1i), indicating a chiral control process of interfacial re-assembly. A morphological statistical analysis gave an average outer diameter of $3.3 \pm 0.2 \mu\text{m}$ and a toroidal width of $1.4 \pm 0.2 \mu\text{m}$ (Fig. 1j and Supplementary Figs. 16 and 17). The average length of the helically arranged nanorod-like subunits along the microtoroidal surface was about $420 \pm 73 \text{ nm}$ (Fig. 1k and Supplementary Figs. 18 and 19). These helical microtoroidal structures could be prepared on varied substrates including silica wafer, glass, mica and quartz plate with similar outer diameters and subunit length (Supplementary Fig. 20), thus representing a universal approach for the preparation of helicity-controlled helical microtoroids.

Characterization of molecular aggregates in solution

The formation of molecular aggregates via a solution-cooling protocol was verified by a series of experiments. The cryogenic capture of the intermediate aggregates in cooled BU MeOH solution (293 K) gave both discrete nanoparticles (diameter, ~45 nm) and predominant nanoparticle-fused aggregates (length, ~220 nm), as observed from the cryo-TEM image (Fig. 2a), indicating the colloidal nature of the supersaturated BU solution after the cooling protocol³⁷. An obvious Tyndall effect (Fig. 2b, inset; Supplementary Fig. 10) and dynamic light

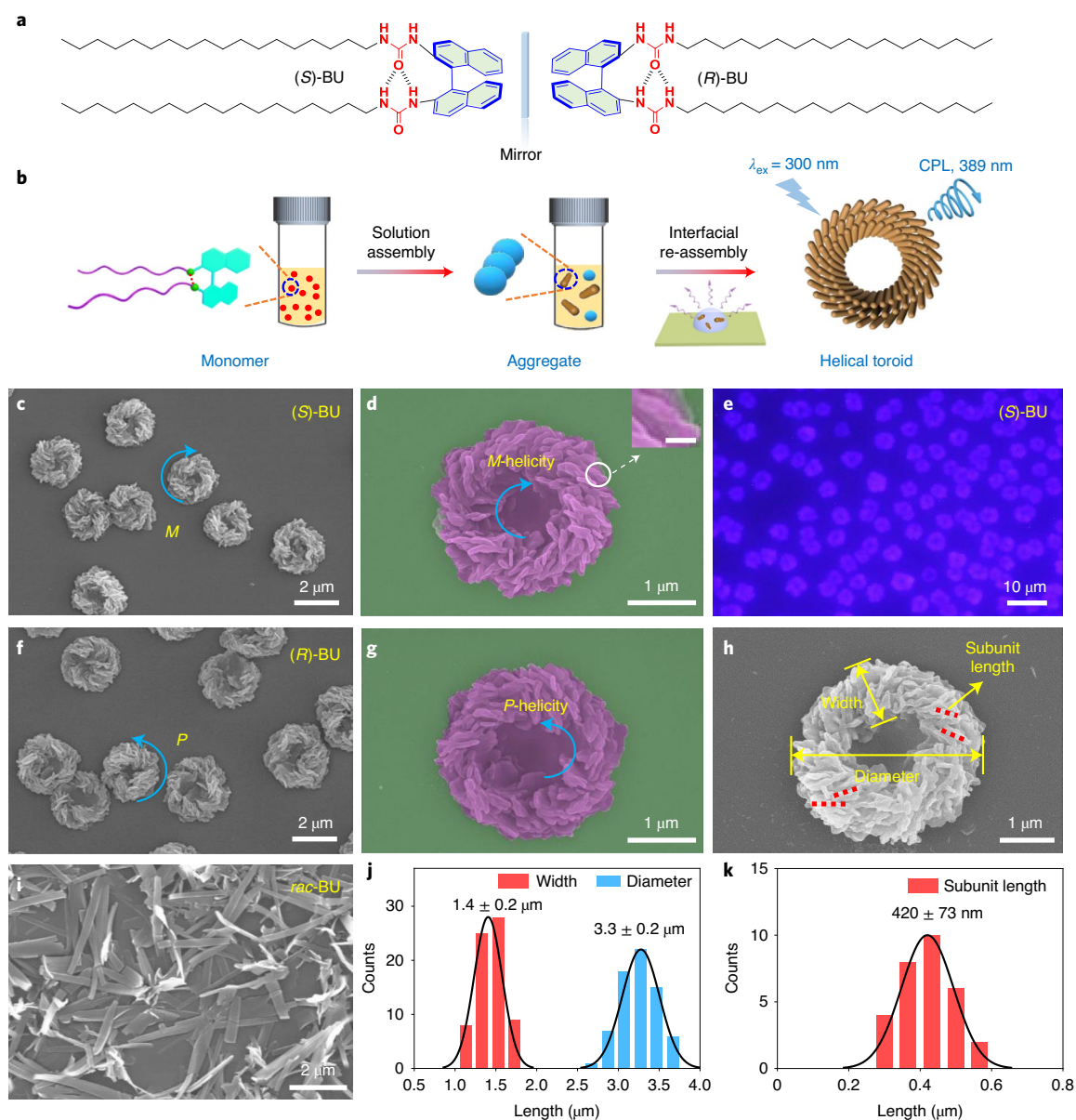


Fig. 1 | Schematic of forming helical microtoroids and morphological analysis. **a**, Chemical structures of binaphthalene BU enantiomers (*S*)-BU and (*R*)-BU, showing an intramolecular hydrogen bond between two urea groups. **b**, Illustration of the stepwise solution self-assembly of BU in supersaturated MeOH (4 mM) and interfacial re-assembly of the aggregates by natural evaporation on a surface. Expansion scale bar is 100 nm. **c–e**, SEM images (**c,d**) and fluorescence microscopy image (**e**) of (*S*)-BU interfacial assemblies on a silica

wafer surface. **f,g**, SEM images of (*R*)-BU interfacial assemblies. **h**, Illustration of morphological parameters (diameter, width and subunit length) of an (*S*)-BU microtoroid. **i**, SEM image of interfacial assemblies from *rac*-BU. **j,k**, Statistical analysis of toroidal width, diameter and subunit length. The cyan arrows in **c, d, f** and **g** highlight the helicity direction of microtoroids. Here *M* and *P* represent left and right handedness, respectively.

scattering (DLS) data at 293 K also clearly supported the formation of particles with sizes of about 228 ± 88 nm (Fig. 2b), which was in the same length scale as the cryogenic aggregates but obviously shorter than the microtoroid subunits (~ 420 nm; Fig. 1k and Supplementary Fig. 20d,h,i). The fast spin coating of the BU intermediate colloids on a silica wafer substrate also afforded similar microtoroids with outer diameters of about $3.5 \mu\text{m}$ and periphery subunits with a length of about 399 ± 43 nm (Fig. 2e and Supplementary Figs. 21 and 22). These data demonstrated that the nanoscale aggregates underwent further morphological evolution and hierarchical self-assembly when they were transferred to the substrate. A magnified SEM image of an interfacial microtoroid clearly showed the tendency of nanoparticle

fusion within a periphery subunit (Fig. 1d, inset). The cryo-TEM morphology observation indicated that the BU solution aggregates were affected by solvent types and different cooling speeds (Supplementary Figs. 23 and 24).

A spectroscopic analysis was conducted to obtain insights into the solution-phase aggregation process. Variable-temperature NMR measurements of the BU solution (4 mM in CD_3OD) provided the in situ aggregation information. On cooling from 343 to 293 K, the chemical-shift range of aromatic protons on naphthalene became broader with ‘proton a’ and ‘proton f’ (Supplementary Fig. 26) moving downfield and upfield, respectively, demonstrating that the naphthalene rings were under the influence of both shielding and deshielding

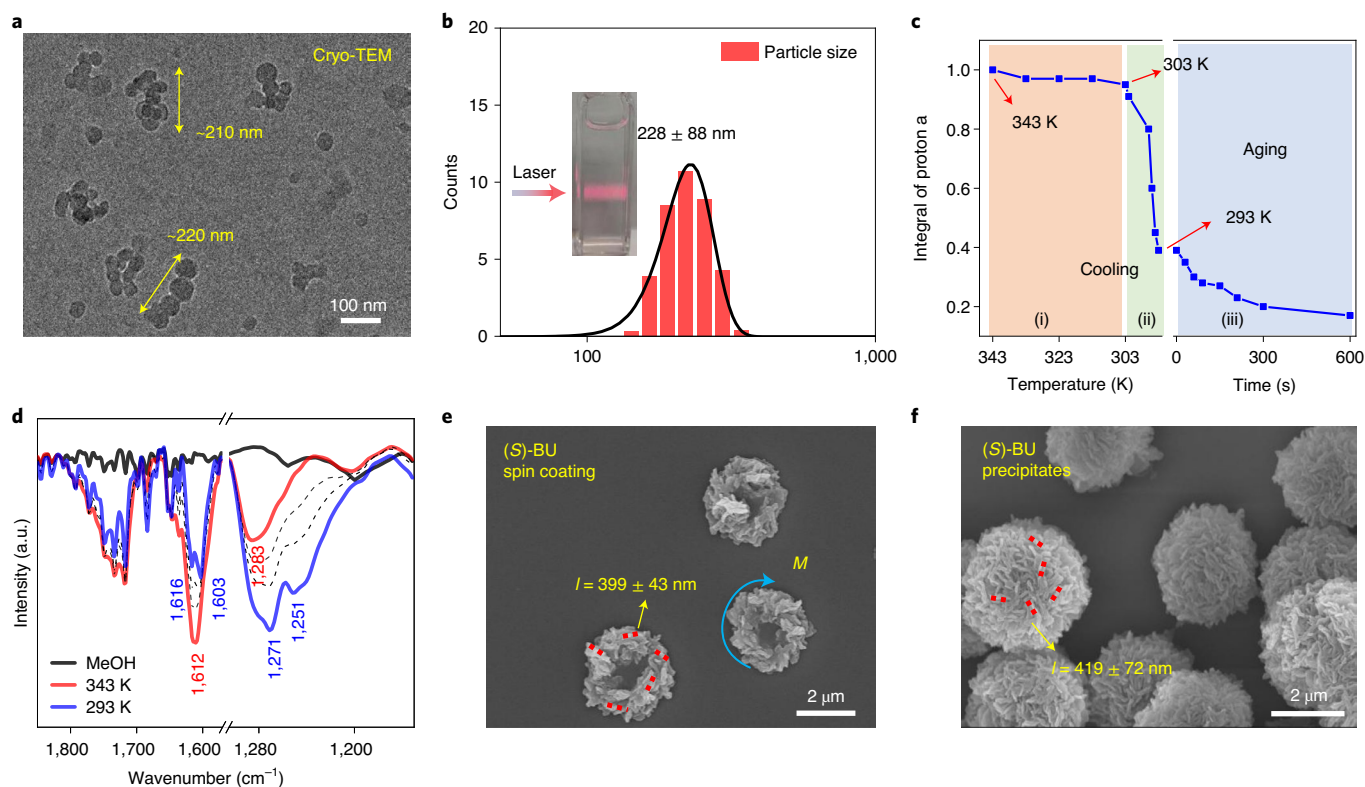


Fig. 2 | Evidence of solution aggregate formation. **a**, Cryo-TEM of vitrified MeOH solution of (S)-BU after cooling to 293 K. **b**, DLS data of (S)-BU supersaturated solution after cooling to 293 K. Inset: photograph of the Tyndall effect under a beam of red light. **c**, Plot of NMR integrals of 'proton a' (Supplementary Fig. 1 shows the proton assignment) against temperature and aging time obtained from variable-temperature NMR of (S)-BU in CD₃OD. Sections (i)–(iii) and the corresponding colours are used to highlight three

different stages. **d**, Variable-temperature FT-IR spectroscopy of (S)-BU solution (8 mM in MeOH). The black dashed lines are the intermediate curves between 293 and 343 K. The black solid line corresponds to the FT-IR signals of bulk MeOH at 293 K. **e**, SEM image of the spin-coated film of the solution aggregates (1,000 rpm, 60 s). **f**, SEM image of the precipitates after aging the solution aggregates over 10 min. Unless otherwise noted, the concentration of BU is 4 mM in MeOH.

effects, which might originate from the alteration of binaphthalene dihedral angle and π - π -stacking interactions³⁸. By using an internal standard method, we were able to evaluate the change in aromatic proton integrals during the aggregation process. The first stage of cooling from 343 to 303 K gave rise to slightly decreased integrals of 'proton a' (Fig. 2c), which demonstrated that NMR-recordable BU monomers or oligomers were the major species in this temperature range. Subsequent cooling from 303 to 293 K induced an obvious decrease in the NMR integrals owing to the formation of NMR-invisible large aggregates, which was in accordance with the cryo-TEM and DLS data. The following aging treatment of the aggregates at 293 K caused a continuous NMR integral decrease owing to further aggregation and formation of precipitates. SEM micrographs showed that these precipitates were micrometre-sized flower-like spheres consisting of several hundreds of nanoscale subunits with length of 419 ± 72 nm (Fig. 2f and Supplementary Fig. 25). Variable-temperature Fourier-transform infrared (FT-IR) spectroscopy of the BU solution showed that the stretching vibration band of the carbonyl group (ν -C=O at $1,612$ cm^{-1}) at a higher temperature (343 K) gradually split into two peaks ($1,616$ and $1,603$ cm^{-1}) on cooling to 293 K, and the bending vibration peak of the N-H bond (δ -N-H, $1,283$ cm^{-1}) was also divided into two peaks centred at $1,271$ and $1,251$ cm^{-1} (Fig. 2d). These splitting peaks suggested the formation of both intra- and intermolecular C=O \cdots H-N hydrogen bonds within the solution aggregates^{39,40}. All these experimental results unambiguously supported the formation of nanoscale molecular aggregates on the controlled cooling protocol of a supersaturated BU hot solution.

Packing modes and proposed self-assembly mechanism

A comparison of the spectroscopic characteristics of BU monomers (BU^{mono}), solution aggregates (BU^{agg}), interfacial microtoroids (BU^{toroid}) and single-crystal structures (BU^{crystal}) could bring useful information for the hierarchical self-assembly mechanism⁴¹. Compared with (S)-BU^{mono} at different concentrations (Fig. 3a and Supplementary Fig. 27), the absorption maximum of the ¹L_a transition for (S)-BU^{toroid} was redshifted from 284 to 300 nm and the intensity of the absorption band above 300 nm was amplified (Fig. 3a), demonstrating an effective chromophore-packing arrangement within the BU interfacial toroids. The emission maximum of (S)-BU^{toroid} also showed a slight bathochromic shift (Fig. 3b). The chiroptical properties of hierarchical structures were studied by circular dichroism (CD) and circularly polarized luminescence (CPL) spectra. The ¹B_b and ¹L_a transitions of BU^{mono} showed opposite Cotton effects due to their perpendicular orientations (Fig. 3c)⁴², which was also confirmed by time-dependent DFT-calculated CD spectrum (Supplementary Fig. 5). Two enantiomers, namely, (S)-BU^{mono} and (R)-BU^{mono}, exhibited mirror-imaged Cotton effects, as expected (Fig. 3c). On formation of the solution aggregates, the Cotton effect of (S)-BU^{agg} at the ¹L_a transition (centred near 284 nm) showed a negative sign, which was in agreement with (S)-BU^{mono}. In sharp contrast, (S)-BU^{toroid} gave rise to a positive Cotton effect (Fig. 3d, blue dashed line; Supplementary Fig. 28b). All the CD spectra calculated using time-dependent density functional theory for different dimeric (S)-BU^{mono} species showed negative Cotton effects at the ¹L_a transition (Supplementary Fig. 29). Therefore, the overall positive

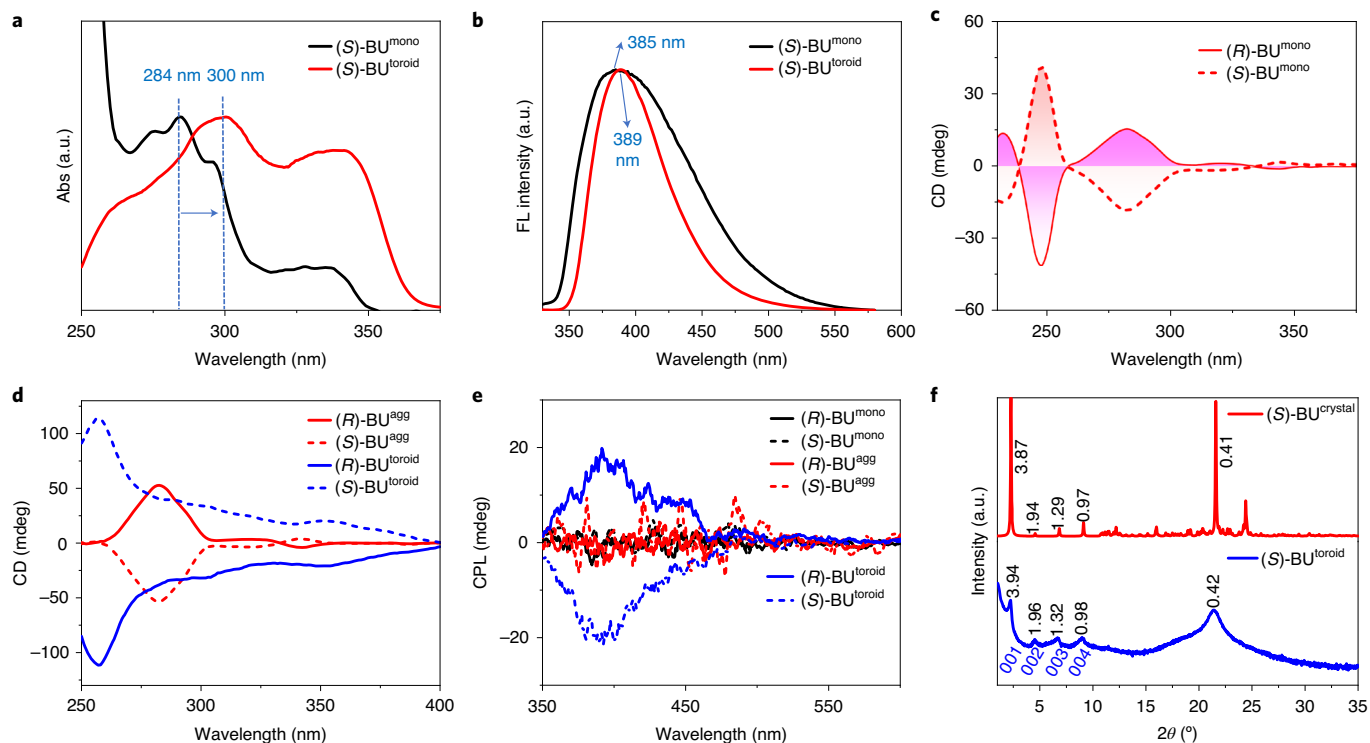


Fig. 3 | Spectroscopic analysis of hierarchical structures. **a, b**, UV-vis absorption (Abs) (**a**) and fluorescence (FL) (**b**) spectra of (S)-BU^{mono} and (S)-BU^{toroid}. The blue arrow indicates the absorption maximum redshift of the ¹L_a transition for (S)-BU^{toroid}. **c**, CD spectra of (S)-BU^{mono} and (R)-BU^{mono}; [BU^{mono}] = 0.2 mM in MeOH, and the cuvette path length is 1 mm. **d**, CD spectra of

BU^{agg} (red lines) and BU^{toroid} (blue lines); [BU^{agg}] = 4 mM in MeOH, and the cuvette path length is 0.1 mm. **e**, CPL spectra of BU^{mono} (black lines), BU^{agg} (red lines) and BU^{toroid} (blue lines); the excitation wavelength is 300 nm. **f**, XRD patterns of (S)-BU^{crystal} (red line) and (S)-BU^{toroid} (blue line).

chiroptical signals of interfacial toroids originated more from the micrometre-sized chiral structures rather than the contribution from monomeric and aggregated species. This conclusion was further unambiguously supported by the CPL spectra because both BU^{mono} and BU^{agg} showed no obvious CPL signals, whereas BU^{toroid} gave an intense CPL emission with luminescent dissymmetry factors (g_{lum}) of 2×10^{-3} (Fig. 3e), which was due to an amplification of structural chirality within the toroidal assemblies⁴³. Therefore, the toroidal organization of solution aggregates on a surface played a critical role in defining the expression of the overall chiroptical properties.

X-ray diffraction (XRD) pattern and infrared spectrum could provide structural information for molecular packing within the assemblies. The XRD pattern of BU microtoroids showed regular diffraction peaks at 2θ values of 2.24° , 4.50° , 6.70° and 8.99° (Fig. 3f). The diffraction peaks calculated from the Bragg's equation gave d -spacing values of 3.94 nm, 1.96 nm, 1.32 nm and 0.98 nm, which should correspond to the (001), (002), (003) and (004) diffractions, respectively (Fig. 3f, blue line), supporting a multilamellar packing mode. In the microtoroid, the CH₂-stretching bands appeared at $2,922\text{ cm}^{-1}$ and $2,851\text{ cm}^{-1}$, thus suggesting the contributions of a gauche conformation of alkyl chains (Supplementary Fig. 30, blue line)⁴⁴. The single-crystal structure provided direct information for the molecular packing mode in the solid state. We successfully obtained the single crystal of (S)-BU by a slow evaporation approach in ethyl acetate/dimethyl sulfoxide co-solvents. The single-crystal XRD data of (S)-BU revealed a triclinic packing diagram with a *P1* chiral space group feature (Fig. 4a and Supplementary Table 1). The intramolecular hydrogen bonds between the two urea groups were retained in the crystal network (Fig. 4b; H...O distances, 2.2 Å and 2.5 Å). A further extension along both *y* and *z* axes was dominated by CH- π interactions (H...C distance, 2.7 Å and 3.0 Å) among neighbouring naphthalene moieties, giving a well-defined

multilamellar structure (Fig. 4a; bilayer length, 3.89 nm). The XRD patterns of the single-crystal and microtoroidal assemblies of (S)-BU showed similar diffraction peaks, therefore proving that BU molecules in the microtoroids adopted similar packing modes to those in the solid structure. However, the diffraction peaks of (S)-BU^{toroid} were obviously broader than those of the single crystal, indicating that the molecular ordering within (S)-BU^{toroid} was not as well defined as that in the crystal, most probably due to the involvement of intermolecular hydrogen bonds, which was in accordance with the variable-temperature FT-IR spectroscopy results.

Atomistic MD simulation using the general AMBER force field (gaff2) was performed to provide insights into the possible self-assembly mechanism. The initial geometrical structure of (S)-BU was extracted from the single-crystal and $5 \times 10 \times 3$ pairs of (S)-BU molecules were generated as one block of cluster (Fig. 4c and Supplementary Fig. 6), which was then solvated in MeOH and equilibrated through MD simulations for 40 ns after thousands of steps of energy minimization. The equilibrium configuration showed that the bilayer packing within the block almost remained, which was in agreement with the XRD pattern. Possible intercluster stacking was also simulated by placing the equilibrated cluster monomer at a distance of -1.5 nm along the *x* axis before solvation in the MeOH solvent (Fig. 4d). The systems for the cluster dimer and trimer containing 600 and 900 (S)-BU molecules were solvated in more than 20,000 and 30,000 MeOH molecules with box sizes of 13.72 nm and 19.72 nm, respectively. After the energy minimization of whole systems, 40 ns MD simulations under the constant pressure/temperature (*NPT*) ensemble were performed. The cluster dimer showed relative translation along the *y* axis, whereas the cluster trimer had an obvious rotation tendency (rotation angle, about 8°) on cluster stacking on top of each other, indicating the preference of circular stacking (Fig. 4e).

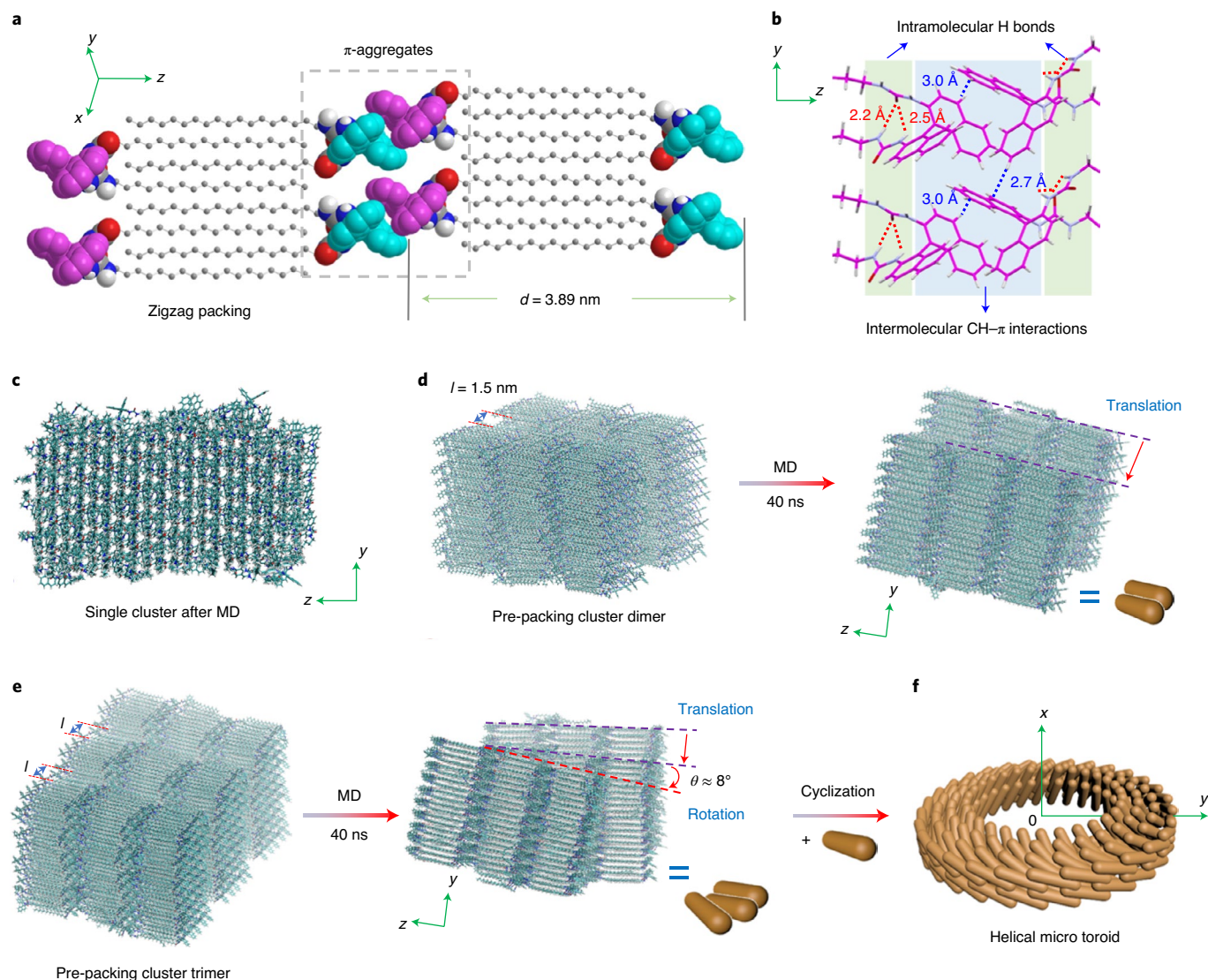


Fig. 4 | Single-crystal structures and MD simulations. **a**, Single-crystal structure of (S)-BU showed well-defined alkane zigzag packing and π -aggregation. **b**, Illustration of intramolecular hydrogen bonds and intermolecular CH- π interactions along two neighbouring bilayers. **c**, Equilibrium structure of a block of clusters containing $5 \times 10 \times 3$ pairs of (S)-BU

molecules after MD simulations. **d**, Pre-packed parallel cluster dimer shows translation along the y axis after 40 ns MD, where l is the distance between two clusters. **e, f**, Pre-packed parallel cluster trimer shows translation and rotation after 40 ns MD (**e**), which then undergoes further circular stacking when interacting with extra clusters (**f**).

Based on these experimental and computational data, we propose a possible aggregation-cyclization mechanism for the formation of interfacial microtoroids. The BU molecules in a supersaturated solution first form discrete and fused nanoparticles (aggregates) on cooling treatment, as supported by the cryo-TEM characterization data through synergistic CH- π interaction, H-bond and alkyl-chain packing. When these aggregates are placed on a substrate, solvent evaporation allows further interaggregate fusion and promotes the formation of nanoscale rod-like structures. The chiral control of interfacial tension drives the helical tilting and cyclization of nanorods, lowering the area of substrate-nanorod interface and facilitating the formation of micrometre-scale helical toroids (Fig. 4f). This mechanism was also verified by control experiments. The directional inter-nanorod interactions revealed by MD simulation should guide further self-assembly on adding extra aggregates. When transferring a second droplet of BU colloids containing molecular aggregates to cover the pre-formed microtoroid domain on silica wafer (Supplementary Fig. 31a), the toroidal topology of interfacial assemblies after natural evaporation

almost remained but with more crowded subunits, leading to increased sizes of toroid diameter (Supplementary Fig. 31e). These results unambiguously indicated that the second batch of aggregates continued to assemble on the helical surface of the previous microtoroids, instead of assembling into new microtoroids, confirming effective inter-nanorod interactions.

Energy transfer within acceptor-doped microtoroids

The chiral microtoroids composed of luminescent chromophores resemble the crystal structure of natural light-harvesting antenna complex¹⁵. We decided to investigate whether the helical toroids can sensitize the guest dye and thus provide a platform for proof-of-concept light-harvesting antenna mimicking both chirality and circularity features (Fig. 5a)⁴⁵. A luminescent phosphoric acid compound was screened out as the acceptor dye due to its spectral overlap and co-assembly ability with the donor BU (Fig. 5b, blue dashed line and red solid line), which enables the possibility of Förster resonance

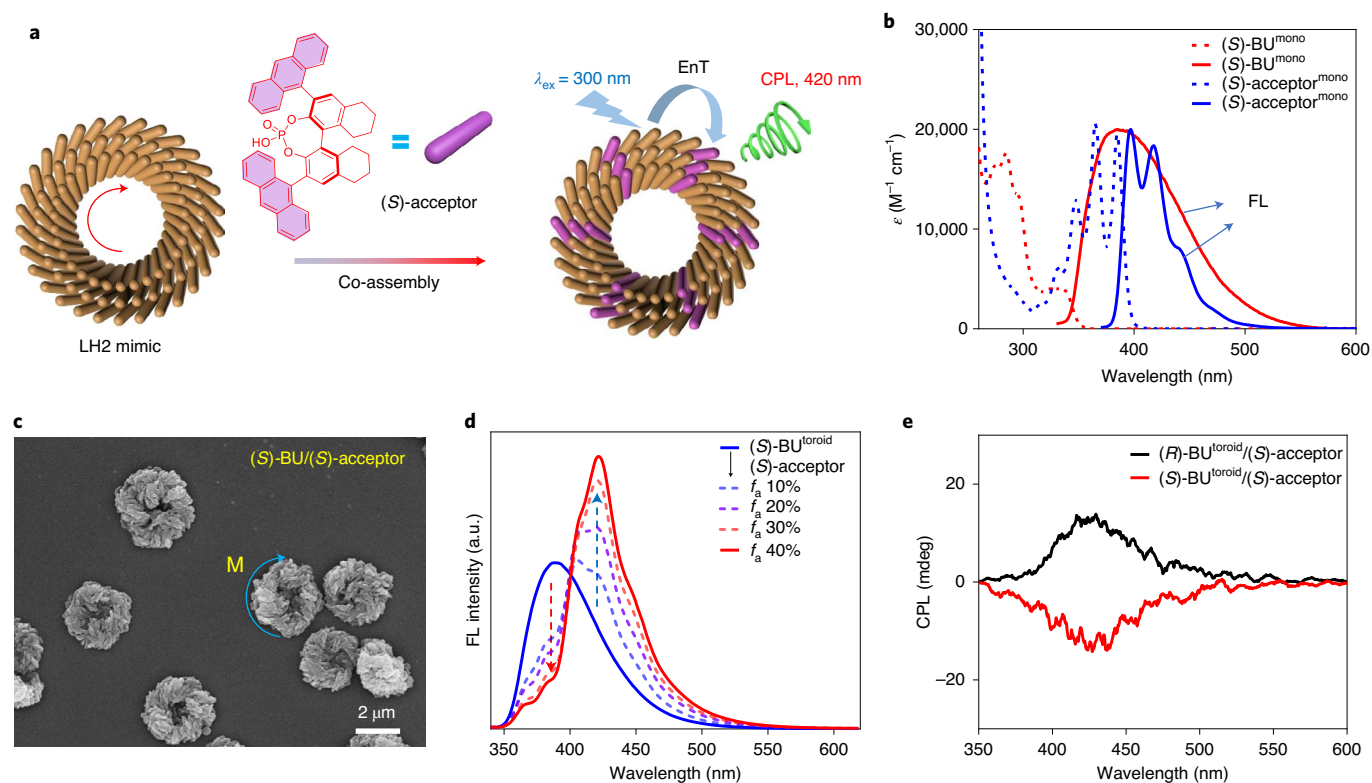


Fig. 5 | Acceptor-dye-doping experiments. **a**, Helical toroid resembles the crystal structure of LH2 and thus is used to co-assemble with a chiral acceptor dye, leading to efficient energy transfer among the two components and circularly polarized luminescence from the acceptor. EnT, energy transfer. **b**, UV-vis absorption (dashed lines) and emission spectra (solid lines) of (S)-BU^{mono} and (S)-acceptor^{mono} in dilute MeOH, showing spectral overlap between donor emission (red solid line) and acceptor absorption (blue dashed

line); the emission spectra are normalized to the absorption maximum of (S)-acceptor^{mono} at 385 nm. **c**, SEM image of (S)-BU/(S)-acceptor interfacial microtoroids. **d**, Fluorescence spectra of (S)-BU/(S)-acceptor microtoroids in the presence of increasing (S)-acceptor ratios (f_a). **e**, CPL spectra of (R)-BU/(S)-acceptor and (S)-BU/(S)-acceptor microtoroids (f_a , 40%). For fluorescence and CPL, the excitation wavelength is 300 nm.

energy transfer within the co-assembled artificial antenna⁴⁶. The addition of acceptor dye (S)-BU or (R)-BU acceptors to (S)-BU or (R)-BU donors exerted no obvious influence on the toroidal topology and helicity of nanostructures, as observed from the SEM and fluorescence microscopy images (Fig. 5c and Supplementary Figs. 33–36), indicating that the arrangement of chiral acceptor dyes followed the helical direction of BU interfacial assemblies. However, the chirality match between the acceptor and BU helical microtoroids could affect the energy transfer and chiroptical properties of their interfacial co-assemblies.

The Förster resonance energy transfer efficiency (Φ_{ET}) in the (S)-BU^{toroid}/(S)-acceptor system was slightly different from the (R)-BU^{toroid}/(S)-acceptor system for acceptor loading ratios (f_a) below 30% (Fig. 5d and Supplementary Fig. 37). The Φ_{ET} value could be improved to over 90% at a relatively high f_a value of 40% (Supplementary Fig. 38), whereas lower f_a values gave less satisfactory energy transfer efficiencies. The sign of chiroptical signals of the co-assembled antenna was defined by the helicity direction of microtoroids; thus, (S)-BU^{toroid}/(S)-acceptor gave the same handedness of the CD signal as the (S)-BU^{toroid} (Supplementary Fig. 39, red line, and Fig. 3d, blue dashed line). The presence of a chiral acceptor dye only affected the spectral position and intensity of the Cotton effect of the diastereomeric pairs of (S)-BU^{toroid}/(S)-acceptor and (R)-BU^{toroid}/(S)-acceptor (Supplementary Fig. 39). When an acceptor dye with the energy match was captured by the microtoroid, Förster resonance energy transfer occurred as in many other cases⁴⁷. However, since the system was chiral, energy-transfer-mediated CPL signal

ascribed to the acceptor was successfully obtained with a $|g_{lum}|$ value of 2×10^{-3} (Fig. 5e)⁴⁸. The structure–property relationship was further elaborated by energy transfer and CPL studies in other solvent systems. Despite the fact that energy transfer could also occur in most of the non-toroidal interfacial assemblies by using other solvents, all of them failed to give energy-transfer-related CPL signals from the acceptor dye (Supplementary Fig. 40), thus again indicating the unique role of toroidal topology in defining the expression of overall chiroptical functions.

Conclusion

In summary, we have shown a combined solution and interface-guided chiral assembly strategy to achieve helical toroidal structures at the micrometre scale. The helicity of toroids is governed by the stereogenic configuration of BU molecules, adopting a chiral control principle of interfacial tension. Morphological analyses, spectroscopic data and computational simulations supported an aggregation–cyclization mechanism for the formation of interfacial microtoroids. The operationally simple method could afford monodispersed micrometre toroids on varied substrates due to improved morphological stability, which provides a powerful alternative approach to the limited existing methods for generating helical toroids. Furthermore, these microtoroids could emit circularly polarized luminescence and exhibit excellent host ability to accommodate guest dyes without structural deformation, in a light-harvesting toroid construct. We believe that the interfacial self-assembly protocol by drop-evaporation or fast spin-coating approaches of pre-formed solution aggregates

will lead to the directed hierarchical chiral self-assembly of numerous functional colloidal dispersion systems, highlighting the prospect of larger-sized chiral superstructures with advanced topology features. These micrometre-scale structures reach a higher scale of chiral self-assembly materials compared with prevailing homochiral architectures at molecular scales or nanoscales.

Online content

Any methods, additional references, Nature Research reporting summaries, source data, extended data, supplementary information, acknowledgements, peer review information; details of author contributions and competing interests; and statements of data and code availability are available at <https://doi.org/10.1038/s41565-022-01234-w>.

References

1. Janoschek, R. *Chirality: From Weak Bosons to the A-Helix* 1st edn (Springer Verlag, 1991).
2. Yashima, E. et al. Supramolecular helical systems: helical assemblies of small molecules, foldamers, and polymers with chiral amplification and their functions. *Chem. Rev.* **116**, 13752–13990 (2011).
3. Kim, J. Y. & Kotov, N. A. Origin of chiroptical activity in nanorod assemblies. *Science* **365**, 1378–1379 (2019).
4. Levin, A. et al. Biomimetic peptide self-assembly for functional materials. *Nat. Rev. Chem.* **4**, 615–634 (2020).
5. Forgan, R. S., Sauvage, J. P. & Stoddart, J. F. Chemical topology: complex molecular knots, links, and entanglements. *Chem. Rev.* **111**, 5434–5464 (2011).
6. Yagai, S., Kitamoto, Y., Datta, S. & Adhikari, B. Supramolecular polymers capable of controlling their topology. *Acc. Chem. Res.* **52**, 1325–1335 (2019).
7. Zhang, W., Jin, W., Fukushima, T., Mori, T. & Aida, T. Helix sense-selective supramolecular polymerization seeded by a one-handed helical polymeric assembly. *J. Am. Chem. Soc.* **137**, 13792–13795 (2015).
8. Palmer, L. C. & Stupp, S. I. Molecular self-assembly into one-dimensional nanostructures. *Acc. Chem. Res.* **41**, 1674–1684 (2008).
9. Morrow, S. M., Bissette, A. J. & Fletcher, S. P. Transmission of chirality through space and across length scales. *Nat. Nanotechnol.* **12**, 410–419 (2017).
10. Cantekin, S., Balkenede, D. W. R., Smulders, M. M. J., Palmans, A. R. A. & Meijer, E. W. The effect of isotopic substitution on the chirality of a self-assembled helix. *Nat. Chem.* **3**, 42–46 (2011).
11. Jones, C. D. et al. Braiding, branching and chiral amplification of nanofibres in supramolecular gels. *Nat. Chem.* **11**, 375–381 (2019).
12. De, S. et al. Designing cooperatively folded abiotic uni- and multimolecular helix bundles. *Nat. Chem.* **10**, 51–57 (2018).
13. Ma, W. et al. Chiral inorganic nanostructures. *Chem. Rev.* **117**, 8041–8093 (2017).
14. Datta, S. et al. Self-assembled poly-catenanes from supramolecular toroidal building blocks. *Nature* **583**, 400–405 (2020).
15. McDermott, G. et al. Crystal structure of an integral membrane light-harvesting complex from photosynthetic bacteria. *Nature* **314**, 517–521 (1995).
16. Avrahami, E. M., Houben, L., Aram, L. & Gal, A. Complex morphologies of biogenic crystals emerge from anisotropic growth of symmetry-related facets. *Science* **376**, 312–316 (2022).
17. Geng, Z. et al. Möbius strips of chiral block copolymers. *Nat. Commun.* **10**, 4090 (2019).
18. Sasaki, N. et al. Supramolecular double-stranded Archimedean spirals and concentric toroids. *Nat. Commun.* **11**, 3578 (2020).
19. Chow, H. Y., Zhang, Y., Matheson, E. & Li, X. Ligation technologies for the synthesis of cyclic peptides. *Chem. Rev.* **119**, 9971–10001 (2019).
20. Laurent, B. A. & Grayson, S. M. Synthetic approaches for the preparation of cyclic polymers. *Chem. Soc. Rev.* **38**, 2202–2213 (2009).
21. Pochan, D. J. et al. Toroidal triblock copolymer assemblies. *Science* **306**, 94–97 (2004).
22. Lee, J. et al. Hollow nanotubular toroidal polymer microrings. *Nat. Chem.* **6**, 97–103 (2014).
23. Frederix, P. W. J. M. et al. Structural and spectroscopic properties of assemblies of self-replicating peptide macrocycles. *ACS Nano* **11**, 7858–7868 (2017).
24. Gagnon, C. et al. Biocatalytic synthesis of planar chiral macrocycles. *Science* **367**, 917–921 (2020).
25. Huang, Z. et al. Pulsating tubules from noncovalent macrocycles. *Science* **337**, 1521–1526 (2012).
26. Chen, J. et al. Artificial muscle-like function from hierarchical supramolecular assembly of photoresponsive molecular motors. *Nat. Chem.* **10**, 132–138 (2018).
27. Dong, A., Chen, J., Vora, P. M., Kikkawa, J. M. & Murray, C. B. Binary nanocrystal superlattice membranes self-assembled at the liquid–air interface. *Nature* **466**, 474–477 (2010).
28. Sun, L. et al. Double-shelled hollow rods assembled from nitrogen/sulfur-codoped carbon coated indium oxide nanoparticles as excellent photocatalysts. *Nat. Commun.* **10**, 2270 (2019).
29. Xia, Y. et al. Self-assembly of self-limiting monodisperse supraparticles from polydisperse nanoparticles. *Nat. Nanotechnol.* **6**, 580–587 (2011).
30. Zheng, Y. et al. Interfacial assembly of dendritic microcapsules with host–guest chemistry. *Nat. Commun.* **5**, 5572 (2014).
31. Walker, D. A., Hedrick, J. L. & Mirkin, C. A. Rapid, large-volume, thermally controlled 3D printing using a mobile liquid interface. *Science* **366**, 360–364 (2019).
32. Gibaud, T. et al. Reconfigurable self-assembly through chiral control of interfacial tension. *Nature* **481**, 348–351 (2012).
33. Sun, M. & Lee, M. Switchable aromatic nanopore structures: functions and applications. *Acc. Chem. Res.* **54**, 2959–2968 (2021).
34. Xu, P. et al. Polymeric toroidal self-assemblies: diverse formation mechanisms and functions. *Adv. Func. Mater.* **32**, 2106036 (2022).
35. Ouyang, G., Ji, L., Jiang, Y., Würthner, F. & Liu, M. Self-assembled Möbius strips with controlled helicity. *Nat. Commun.* **11**, 5910 (2020).
36. Song, S. et al. The role of cooling rate in crystallization-driven block copolymer self-assembly. *Chem. Sci.* **13**, 396–409 (2022).
37. Ruiz-Carretero, A. et al. Stepwise self-assembly to improve solar cell morphology. *J. Mater. Chem. A* **1**, 11674 (2013).
38. Parenti, F., Tassinari, F., Libertini, E., Lanzi, M. & Mucci, A. π -stacking signature in NMR solution spectra of thiophene-based conjugated polymers. *ACS Omega* **2**, 5775–5784 (2017).
39. Aida, T., Meijer, E. W. & Stupp, S. I. Functional supramolecular polymers. *Science* **335**, 813–817 (2012).
40. Wehner, M. et al. Supramolecular polymorphism in one-dimensional self-assembly by kinetic pathway control. *J. Am. Chem. Soc.* **141**, 6092–6107 (2019).
41. Babu, S. S., Praveen, V. K. & Ajayaghosh, A. Functional π -gelators and their applications. *Chem. Rev.* **114**, 1973–2129 (2014).
42. Harada, N. & Nakanishi, K. A method for determining the chirality of two aromatic chromophores and the absolute configurations of chromomycin A3 and related antibiotics. *J. Am. Chem. Soc.* **91**, 5896–5898 (1969).

43. Liu, M., Zhang, L. & Wang, T. Supramolecular chirality in self-assembled systems. *Chem. Rev.* **115**, 7304–7397 (2015).
44. Ang, T. P., Wee, T. S. A. & Chin, W. S. Three-dimensional self-assembled monolayer (3D SAM) of *n*-alkanethiols on copper nanoclusters. *J. Phy. Chem. B.* **108**, 11001–11010 (2004).
45. Scholes, G. D., Fleming, G. R., Olaya-Castro, A. & van Grondelle, R. Lessons from nature about solar light harvesting. *Nat. Chem.* **3**, 763–774 (2011).
46. Ajayaghosh, A., Praveen, V. K. & Vijayakumar, C. Organogels as scaffolds for excitation energy transfer and light harvesting. *Chem. Soc. Rev.* **37**, 109–122 (2008).
47. Wasielewski, M. R. Self-assembly strategies for integrating light harvesting and charge separation in artificial photosynthetic systems. *Acc. Chem. Res.* **42**, 1910–1921 (2009).
48. Hall, J., Renger, T., Picorel, R. & Krausz, E. Circularly polarized luminescence spectroscopy reveals low-energy excited states and dynamic localization of vibronic transitions in CP43. *Biochim. Biophys. Acta Bioenerg.* **1857**, 115–128 (2016).

Publisher's note Springer Nature remains neutral with regard to jurisdictional claims in published maps and institutional affiliations.

Open Access This article is licensed under a Creative Commons Attribution 4.0 International License, which permits use, sharing, adaptation, distribution and reproduction in any medium or format, as long as you give appropriate credit to the original author(s) and the source, provide a link to the Creative Commons license, and indicate if changes were made. The images or other third party material in this article are included in the article's Creative Commons license, unless indicated otherwise in a credit line to the material. If material is not included in the article's Creative Commons license and your intended use is not permitted by statutory regulation or exceeds the permitted use, you will need to obtain permission directly from the copyright holder. To view a copy of this license, visit <http://creativecommons.org/licenses/by/4.0/>.

© The Author(s) 2022

Methods

Materials

All the commercial chemicals were used as received without further purification. The synthesis procedures of (S)-BU, (R)-BU and *rac*-BU are listed in Supplementary Scheme 1. The reference BU compounds, namely, (S)-BU-C4, (S)-BU-C7, (S)-BU-C11 and (S)-BU-Me, are listed in Supplementary Scheme 2.

Interfacial assembly protocol

Typically, 1.75 mg (2 μ mol) BU was dispersed into 0.5 ml MeOH in a 3 ml sample vial or cuvette. The mixture was heated at 343 K until the solid was entirely dissolved. The solution was cooled from 343 K to 293 K at a speed of 5 K min⁻¹ with a UH4150 (Hitachi) variable-temperature accessory. A drop of the cooled solution was then transferred to the target substrate (291 K) via a syringe. After natural evaporation at room temperature (293 K), interfacial assemblies were obtained and used for further measurements.

SEM, atomic force microscopy and TEM characterizations

SEM measurement was performed on an S4800 (Hitachi) instrument with an accelerating voltage of 10 kV and a working current of 10 μ A. The atomic force microscopy image was recorded on a Dimension FastScan (Bruker Nano) instrument with a silicon tip on silicon nitride cantilevers in the tapping mode (30 μ m length with typical resonant frequencies of 400 kHz and spring constant of 4 N m⁻¹). TEM was performed on a JEM-1011 (JEOL) instrument with an accelerating voltage of 100 kV. Cryo-TEM was performed on a Themis300 (Thermo Scientific) instrument with an accelerating voltage of 200 kV or 300 kV.

UV-vis spectroscopy

The solution samples were loaded in a quartz cuvette to record the UV-vis absorption spectra on a U-3900 (Hitachi) spectrophotometer. To avoid scattering effects originating from the large size of these microstructures, the solid samples were removed from the substrates with a scraper and were transferred to a BaSO₄ sample plate, which was then measured through the UV-vis diffuse-reflectance spectrum mode on a UV-2600 (Shimadzu) spectrophotometer.

Fluorescence spectrum

The fluorescence spectra were recorded on an F-4500 fluorescence spectrophotometer (Hitachi) at a voltage of 400 V with a 5 nm slit for both excitation and emission sides. Fluorescence decay curves were recorded on an FLS980 (Edinburgh Instruments) spectrophotometer. The fluorescence quantum yields were measured on a FluoroMax Plus (HORIBA) instrument by using an integrating sphere.

CD spectrum

The electronic circular dichroism and linear dichroism spectra were simultaneously recorded on a CD spectrometer J-1500 (JASCO) at a scanning rate of 500 nm min⁻¹ in the range of -200–650 nm (solution, transmission mode) or -250–650 nm (solid, diffuse-reflectance mode).

CPL

The CPL spectra were recorded on a CPL-300 spectrophotometer (JASCO) in the range of -350–600 nm. The excitation wavelength for all the samples was 300 nm. The g_{lum} spectra were transferred from the CPL spectra using the Spectra Manager software of JASCO (Version 2.12.00).

Fluorescence microscopy image

The interfacial assemblies were observed on an IX83 (Olympus) fluorescence microscope.

FT-IR spectrum

The ground solid samples were dispersed in a KBr pellet and submitted for FT-IR spectra measurement on Bruker Tensor 27. The liquid samples were measured on a VERTEX 70v (Bruker) FT-IR instrument.

Powder and single-crystal XRD measurements

The solid samples were directly loaded onto a glass sample holder to record the XRD spectra on EmpyreanX (PANalytical) with Cu-K α radiation ($\lambda = 1.5406 \text{ \AA}$) at 40 kV and 40 mA. The scanning range was from 1° to 60°. Single-crystal XRD was performed by an XtaLAB Synergy-R (Rigaku) diffractometer.

NMR and mass spectra

Here ¹H NMR, ¹³C NMR, COSY and ROESY spectra were measured on Bruker Avance spectrometers (Bruker BioSpin) with CD₃OD, CDCl₃ or acetone-d₆ as the solvents. Matrix-assisted laser desorption/ionization Fourier-transform ion cyclotron resonance mass spectrometry was performed on an ultrafleXtreme (Bruker) mass spectrometer.

High-performance liquid chromatography

The samples were measured on Waters 1525 binary HPLC pump with an analytical chiral column CHIRALPAK AD-H (5 μ m), and an isopropanol/hexane mixture was used as the mobile phase.

DLS

The samples were measured at 293 K by a Zetasizer Nano ZS ZEN3600 instrument (Malvern Instruments).

DFT computation

The energy-optimized structures were obtained by DFT computation at the B3LYP 6-311 + g(d,p) level of theory. The absorption and CD spectra were calculated by time-dependent DFT methods⁴⁹.

MD simulations

Atomistic MD simulations have been performed in the GROMACS (version 2020.6) simulation package using gaff2. The temperature was coupled to 298 K using the Nosé–Hoover method and the pressure was coupled to 1 atm using the Parrinello–Rahman method. The cutoff scheme of 1.2 nm was implemented for the non-bonded interactions, and the particle mesh Ewald method with a Fourier spacing of 0.1 nm was applied for the long-range electrostatic interactions. All the covalent bonds with hydrogen atoms were constrained using the linear constraint solver algorithm.

Reporting summary

Further information on research design is available in the Nature Research Reporting Summary linked to this article.

Data availability

All relevant data are available from the corresponding authors on reasonable request. The X-ray crystallographic coordinates for structures reported in this study have been deposited at the Cambridge Crystallographic Data Centre (CCDC) under deposition numbers [2203258](#) for (S)-BU and [2203259](#) for *rac*-BU. These data can be obtained free of charge from the CCDC via http://www.ccdc.cam.ac.uk/data_request/cif. Source data are provided with this paper.

References

49. Frisch, M. J. et al. Gaussian 09, revision D.01 (Gaussian, 2013).

Acknowledgements

This work was financially supported by the National Natural Science Foundation of China (21890734 and 21890730 for M.L.; 21971247 for G.O.), Youth Innovation Promotion Association of CAS (2019036 for

G.O.), BMS Junior Fellow of BNLMS (2019BMS20010 for C.D.) and the China Postdoctoral Science Foundation (2020M670464 for C.D.). We thank L. Zhang and H. Wang for helpful discussions. We thank B. Guan and J. Yue for the cryo-TEM measurements.

Author contributions

M.L. conceived the idea and supervised the project. C.D., G.O., X.Z. and Z.L. designed the experiments. C.D. and Z.L. carried out the experiments. G.O. performed the DFT computations. The manuscript was written by G.O. and M.L. with inputs from all the authors.

Competing interests

The authors declare no competing interests.

Additional information

Supplementary information The online version contains supplementary material available at <https://doi.org/10.1038/s41565-022-01234-w>.

Correspondence and requests for materials should be addressed to Guanghui Ouyang or Minghua Liu.

Peer review information *Nature Nanotechnology* thanks Shiki Yagai and the other, anonymous, reviewer(s) for their contribution to the peer review of this work.

Reprints and permissions information is available at www.nature.com/reprints.

Reporting Summary

Nature Portfolio wishes to improve the reproducibility of the work that we publish. This form provides structure for consistency and transparency in reporting. For further information on Nature Portfolio policies, see our [Editorial Policies](#) and the [Editorial Policy Checklist](#).

Statistics

For all statistical analyses, confirm that the following items are present in the figure legend, table legend, main text, or Methods section.

- | n/a | Confirmed |
|-------------------------------------|--|
| <input type="checkbox"/> | <input checked="" type="checkbox"/> The exact sample size (n) for each experimental group/condition, given as a discrete number and unit of measurement |
| <input type="checkbox"/> | <input checked="" type="checkbox"/> A statement on whether measurements were taken from distinct samples or whether the same sample was measured repeatedly |
| <input type="checkbox"/> | <input checked="" type="checkbox"/> The statistical test(s) used AND whether they are one- or two-sided
<i>Only common tests should be described solely by name; describe more complex techniques in the Methods section.</i> |
| <input type="checkbox"/> | <input checked="" type="checkbox"/> A description of all covariates tested |
| <input checked="" type="checkbox"/> | <input type="checkbox"/> A description of any assumptions or corrections, such as tests of normality and adjustment for multiple comparisons |
| <input type="checkbox"/> | <input checked="" type="checkbox"/> A full description of the statistical parameters including central tendency (e.g. means) or other basic estimates (e.g. regression coefficient) AND variation (e.g. standard deviation) or associated estimates of uncertainty (e.g. confidence intervals) |
| <input checked="" type="checkbox"/> | <input type="checkbox"/> For null hypothesis testing, the test statistic (e.g. F , t , r) with confidence intervals, effect sizes, degrees of freedom and P value noted
<i>Give P values as exact values whenever suitable.</i> |
| <input checked="" type="checkbox"/> | <input type="checkbox"/> For Bayesian analysis, information on the choice of priors and Markov chain Monte Carlo settings |
| <input checked="" type="checkbox"/> | <input type="checkbox"/> For hierarchical and complex designs, identification of the appropriate level for tests and full reporting of outcomes |
| <input checked="" type="checkbox"/> | <input type="checkbox"/> Estimates of effect sizes (e.g. Cohen's d , Pearson's r), indicating how they were calculated |

Our web collection on [statistics for biologists](#) contains articles on many of the points above.

Software and code

Policy information about [availability of computer code](#)

Data collection

Data analysis

For manuscripts utilizing custom algorithms or software that are central to the research but not yet described in published literature, software must be made available to editors and reviewers. We strongly encourage code deposition in a community repository (e.g. GitHub). See the Nature Portfolio [guidelines for submitting code & software](#) for further information.

Data

Policy information about [availability of data](#)

All manuscripts must include a [data availability statement](#). This statement should provide the following information, where applicable:

- Accession codes, unique identifiers, or web links for publicly available datasets
- A description of any restrictions on data availability
- For clinical datasets or third party data, please ensure that the statement adheres to our [policy](#)

All relevant data are available from the authors under reasonable request. Supplementary Information is available in the online version of the paper. Source data for Fig. 1j-1k, 2b-2d, 3a-3f, 5b, 5d, 5e are provided with this paper. The X-ray crystallographic coordinates for structures reported in this study have been deposited

Human research participants

Policy information about [studies involving human research participants and Sex and Gender in Research](#).

Reporting on sex and gender

Use the terms sex (biological attribute) and gender (shaped by social and cultural circumstances) carefully in order to avoid confusing both terms. Indicate if findings apply to only one sex or gender; describe whether sex and gender were considered in study design whether sex and/or gender was determined based on self-reporting or assigned and methods used. Provide in the source data disaggregated sex and gender data where this information has been collected, and consent has been obtained for sharing of individual-level data; provide overall numbers in this Reporting Summary. Please state if this information has not been collected. Report sex- and gender-based analyses where performed, justify reasons for lack of sex- and gender-based analysis.

Population characteristics

Describe the covariate-relevant population characteristics of the human research participants (e.g. age, genotypic information, past and current diagnosis and treatment categories). If you filled out the behavioural & social sciences study design questions and have nothing to add here, write "See above."

Recruitment

Describe how participants were recruited. Outline any potential self-selection bias or other biases that may be present and how these are likely to impact results.

Ethics oversight

Identify the organization(s) that approved the study protocol.

Note that full information on the approval of the study protocol must also be provided in the manuscript.

Field-specific reporting

Please select the one below that is the best fit for your research. If you are not sure, read the appropriate sections before making your selection.

Life sciences Behavioural & social sciences Ecological, evolutionary & environmental sciences

For a reference copy of the document with all sections, see nature.com/documents/nr-reporting-summary-flat.pdf

Life sciences study design

All studies must disclose on these points even when the disclosure is negative.

Sample size

Describe how sample size was determined, detailing any statistical methods used to predetermine sample size OR if no sample-size calculation was performed, describe how sample sizes were chosen and provide a rationale for why these sample sizes are sufficient.

Data exclusions

Describe any data exclusions. If no data were excluded from the analyses, state so OR if data were excluded, describe the exclusions and the rationale behind them, indicating whether exclusion criteria were pre-established.

Replication

Describe the measures taken to verify the reproducibility of the experimental findings. If all attempts at replication were successful, confirm this OR if there are any findings that were not replicated or cannot be reproduced, note this and describe why.

Randomization

Describe how samples/organisms/participants were allocated into experimental groups. If allocation was not random, describe how covariates were controlled OR if this is not relevant to your study, explain why.

Blinding

Describe whether the investigators were blinded to group allocation during data collection and/or analysis. If blinding was not possible, describe why OR explain why blinding was not relevant to your study.

Behavioural & social sciences study design

All studies must disclose on these points even when the disclosure is negative.

Study description

Briefly describe the study type including whether data are quantitative, qualitative, or mixed-methods (e.g. qualitative cross-sectional, quantitative experimental, mixed-methods case study).

Research sample

State the research sample (e.g. Harvard university undergraduates, villagers in rural India) and provide relevant demographic information (e.g. age, sex) and indicate whether the sample is representative. Provide a rationale for the study sample chosen. For studies involving existing datasets, please describe the dataset and source.

Sampling strategy

Describe the sampling procedure (e.g. random, snowball, stratified, convenience). Describe the statistical methods that were used to predetermine sample size OR if no sample-size calculation was performed, describe how sample sizes were chosen and provide a

	<i>rationale for why these sample sizes are sufficient. For qualitative data, please indicate whether data saturation was considered, and what criteria were used to decide that no further sampling was needed.</i>
Data collection	<i>Provide details about the data collection procedure, including the instruments or devices used to record the data (e.g. pen and paper, computer, eye tracker, video or audio equipment) whether anyone was present besides the participant(s) and the researcher, and whether the researcher was blind to experimental condition and/or the study hypothesis during data collection.</i>
Timing	<i>Indicate the start and stop dates of data collection. If there is a gap between collection periods, state the dates for each sample cohort.</i>
Data exclusions	<i>If no data were excluded from the analyses, state so OR if data were excluded, provide the exact number of exclusions and the rationale behind them, indicating whether exclusion criteria were pre-established.</i>
Non-participation	<i>State how many participants dropped out/declined participation and the reason(s) given OR provide response rate OR state that no participants dropped out/declined participation.</i>
Randomization	<i>If participants were not allocated into experimental groups, state so OR describe how participants were allocated to groups, and if allocation was not random, describe how covariates were controlled.</i>

Ecological, evolutionary & environmental sciences study design

All studies must disclose on these points even when the disclosure is negative.

Study description	<i>Briefly describe the study. For quantitative data include treatment factors and interactions, design structure (e.g. factorial, nested, hierarchical), nature and number of experimental units and replicates.</i>
Research sample	<i>Describe the research sample (e.g. a group of tagged <i>Passer domesticus</i>, all <i>Stenocereus thurberi</i> within Organ Pipe Cactus National Monument), and provide a rationale for the sample choice. When relevant, describe the organism taxa, source, sex, age range and any manipulations. State what population the sample is meant to represent when applicable. For studies involving existing datasets, describe the data and its source.</i>
Sampling strategy	<i>Note the sampling procedure. Describe the statistical methods that were used to predetermine sample size OR if no sample-size calculation was performed, describe how sample sizes were chosen and provide a rationale for why these sample sizes are sufficient.</i>
Data collection	<i>Describe the data collection procedure, including who recorded the data and how.</i>
Timing and spatial scale	<i>Indicate the start and stop dates of data collection, noting the frequency and periodicity of sampling and providing a rationale for these choices. If there is a gap between collection periods, state the dates for each sample cohort. Specify the spatial scale from which the data are taken</i>
Data exclusions	<i>If no data were excluded from the analyses, state so OR if data were excluded, describe the exclusions and the rationale behind them, indicating whether exclusion criteria were pre-established.</i>
Reproducibility	<i>Describe the measures taken to verify the reproducibility of experimental findings. For each experiment, note whether any attempts to repeat the experiment failed OR state that all attempts to repeat the experiment were successful.</i>
Randomization	<i>Describe how samples/organisms/participants were allocated into groups. If allocation was not random, describe how covariates were controlled. If this is not relevant to your study, explain why.</i>
Blinding	<i>Describe the extent of blinding used during data acquisition and analysis. If blinding was not possible, describe why OR explain why blinding was not relevant to your study.</i>

Did the study involve field work? Yes No

Reporting for specific materials, systems and methods

We require information from authors about some types of materials, experimental systems and methods used in many studies. Here, indicate whether each material, system or method listed is relevant to your study. If you are not sure if a list item applies to your research, read the appropriate section before selecting a response.

Materials & experimental systems

n/a	Involvement in the study
<input checked="" type="checkbox"/>	<input type="checkbox"/> Antibodies
<input checked="" type="checkbox"/>	<input type="checkbox"/> Eukaryotic cell lines
<input checked="" type="checkbox"/>	<input type="checkbox"/> Palaeontology and archaeology
<input checked="" type="checkbox"/>	<input type="checkbox"/> Animals and other organisms
<input checked="" type="checkbox"/>	<input type="checkbox"/> Clinical data
<input checked="" type="checkbox"/>	<input type="checkbox"/> Dual use research of concern

Methods

n/a	Involvement in the study
<input checked="" type="checkbox"/>	<input type="checkbox"/> ChIP-seq
<input checked="" type="checkbox"/>	<input type="checkbox"/> Flow cytometry
<input checked="" type="checkbox"/>	<input type="checkbox"/> MRI-based neuroimaging